Potential for Small Unmanned Aircraft Systems applications for identifying groundwater-surface water exchange in a meandering river reach

H. Pai[1], H. Malenda[2], M. Briggs[3], K. Singha[2], R. González-Pinzón[4], M. Gooseff[5], S.W. Tyler[1], and the AirCTEMPS Team

[1] Dept. of Geological Sciences and Engineering, University of Nevada, Reno

[2]Hydrologic Science and Engineering Program, Colorado School of Mines, Golden, CO 80401

[3]U.S. Geological Survey, Office of Groundwater, Branch of Geophysics, Storrs CT 06269

[4]Department of Civil Engineering, University of New Mexico, Albuquerque, New Mexico, USA

[5]Institute of Arctic & Alpine Research, University of Colorado, Boulder, CO 80309 USA.

Corresponding author: Henry Pai (henryp@unr.edu)

Key Points:

High-resolution imagery can be obtained from small unmanned aerial systems (sUAS) for riparian, groundwater-surface water exchange analysis.

sUAS-based topographic mapping provides efficient and high-resolution surface-water elevation profiling and breaks in slope.

Hydraulic conductivity and temperature profiling can be used to ground-truth exchange patterns identified with sUAS imagery.

Abstract

The exchange of groundwater and surface water (GW-SW), including dissolved constituents and energy, represents a critical yet challenging characterization problem for hydrogeologists and stream ecologists. Here, we describe the use of a suite of high spatial-resolution remote- sensing techniques, collected using a small unmanned aircraft system (sUAS), to provide novel and complementary data to analyze GW-SW exchange. sUAS provided centimeter- scale resolution topography and water surface elevations, which are often drivers of exchange along the river corridor. Additionally, sUAS-based vegetation imagery, vegetation-top elevation, and normalized difference vegetation index (NDVI) mapping indicated GW-SW exchange patterns that are difficult to characterize from the land surface and may not be resolved from coarser satellite-based imagery. We combined these data with estimates of sediment hydraulic conductivity to provide a direct estimate of GW "shortcutting" through meander necks, which was corroborated by temperature data at the riverbed interface.

Final copy as submitted to Geophysical Research Letters for publication as:
Pai, H., Malenda, H., Briggs, M.A., Singha, K., González-Pinzón, R., Gooseff, M., Tyler, S.W., and AirCTEMPS Team, 2017, Potential for small unmanned aircraft systems applications for identifying groundwater-surface water exchange in a meandering river reach: Geophysical Research Letters, http://doi.org/10.1002/2017GL075836.

Introduction

GW-SW exchange in river corridor systems is an important driver for riverine ecosystem functions. Exchange can govern metabolism and nutrient uptake (Boano et al., 2014; Briggs et al., 2014; González-Pinzón et al., 2014), contaminant attenuation (Broshears et al., 1996; Fuller & Harvey, 2000; Harvey & Fuller, 1998) and thermal regulation for SW habitats (Ebersole et al., 2003; Hare et al., 2015). Generally, we characterize GW-SW systems with intensive field experiments (e.g., González-Pinzón et al., 2015) coupled with physical and systems models describing the study reach (Boano et al., 2014; Briggs et al., 2012; Cardenas, 2015; Knapp et al., 2017). While these physics-based models attempt to account for complexities encountered across spatial scales (e.g., sinuosity, bed morphologies, sediment structure), such models often lack multi-scale measurement validation and, thus, are sensitive to epistemic and parameterization uncertainties (Cardenas, 2015; Gomez-Velez et al., 2015; Harvey & Gooseff, 2015).

Common methods for quantifying GW-SW exchange require time consuming measurements of water surface elevations (WSE), boundary conditions to constrain mass balances (e.g., differential gauging, seepage meters, tracers), energy differences (e.g., hydraulic head), and/or coupled mass or heat transfer (e.g., ambient heat tracers) (Kalbus et al., 2006; Selker et al., 2006). Additional local characteristics affecting flow, mass, and heat transfer processes are also commonly required (e.g., topography, bathymetry, morphology, sediment characterization). In this context, remote-sensing products may alleviate some data collection challenges, especially when exploring reach-scale systems. High-resolution topographic light detection and ranging (LiDAR) data are common for topographic reconstructions (Passalacqua et al., 2015), and for bathymetric products used in hyporheic exchange models (Marzadri et al., 2014). Emerging studies in photogrammetry also show promise for determining WSE and as potential replacements for LiDAR or traditional survey techniques, which are costly in either money or time (Javernick et al., 2014; Woodget et al., 2015). Additionally, satellite-derived products have been recently used to relate shallow GW (Eamus et al., 2015; Jin et al., 2011; Lv et al., 2013; Zhou et al., 2013) and soil moisture (Wang et al., 2007) through 30-m resolution normalized difference vegetation indices (NDVIs). These data could be important for identifying river corridor preferential-flow processes and for exploring how hydrogeomorphology impacts GW-SW exchange (Zhou et al., 2013), particularly across meander necks where vegetation biomass is influenced by the depth to water table (Perucca et al., 2006). Similarly, thermal infrared data have been ground- based (Cardenas et al., 2014) or aerially collected (e.g., Dugdale et al., 2015; Loheide & Gorelick, 2006) to locate GW discharge points at the landscape scale and delineate SW transient storage (Bingham et al., 2012). Recent developments in robust designs of sUAS for delivering various sensor payloads make environmental sensing of surface processes now more accessible to the GW-SW research community (Hare et al., 2015; Whitehead & Hugenholtz, 2014).

For environmental sciences, data products from sUAS remote sensing campaigns can provide high-resolution characterization of terrestrial landscapes, and map aquatic and atmospheric processes. The development of Structure-from-Motion (SfM) techniques for sUAS has revolutionized photogrammetry, with sUAS providing centimeter-scale digital elevation models at a fraction of the cost of traditional photogrammetry. Across the terrestrial landscape, sUAS cameras are deployed for snapshots of vegetation density, distribution, classification, and health states (e.g., Lucieer et al., 2014) or vegetation changes (Zahawi et al., 2015), and for time-series snapshots to estimate snow depth (Vander Jagt et al., 2015).

Such data products provide higher resolution than satellite-derived products, at a scale that is not easily recreated with standard ground-level field methods.

Here, we combine traditional field approaches with developments in sUAS technology to quantify GW-SW exchange and to demonstrate sUAS' synergy for these types of studies. The field experiments focus on sinuosity-driven GW-SW exchange, with "shortcutting" fluxes across meander

necks (e.g., Boano et al., 2006; Revelli et al., 2008).

The East River site is located within the Lawrence Berkeley National Laboratory's Watershed Science Focus Area, near Crested Butte, Colorado, USA (Winnick et al., 2017). sUAS imagery (both visible and near infrared) was used to create low-cost, high-resolution digital elevation and NDVI maps of the river reach. The synthesis of these data generated a high-resolution WSE profile of the river for hydraulic gradient analyses and vegetative characteristics in NDVI to examine GW-SW exchange processes at much higher resolution than traditional ground-based methods.

Materials and Methods

Site information

The East River in south-central Colorado was instrumented in the summer of 2016 as part of a summer workshop on GW-SW exchange (Figure 1a). The river morphology is dominated by meander bends cut into the alluvial riparian corridor, which is underlain by a glacially scoured shale basement. The stream width is typically 10-15 m, with stream depth ranging from shallow riffles to deeper (1-2 m) pools. For a more complete description of the field site, the reader is referred to Winnick et al. (2017) and Kenwell et al. (2016). The site was instrumented for continuous streamflow as well as temperature, fluid conductivity and heads in 28 shallow piezometers. For this work, data from a series of falling-head slug tests at six wells located within our study site were used to estimate sediment hydraulic conductivities. The river flow is dominated by winter snowmelt, and was 0.8 m^3/s during this study. Seasonal river stage fluctuations cause portions of meanders to be inundated (Kenwell et al., 2016) and likely affect riparian vegetation along with varying GW conditions (Perucca et al., 2006).

As part of our experiments, fiber-optic distributed temperature sensing (FO-DTS) was deployed to identify GW discharge to SW. The period from 10 to 31 August 2016 was used to determine summary statistics of temperature along the streambed interface at a 1.01 m spatial scale. A comprehensive description of FO-DTS technology related specifically to

GW-SW exchange research can be found in Hare et al. (2015). We employed a suite of sUAS-derived products and in-situ FO-DTS for identifying field-scale localizations of GW-SW exchange given modeled (e.g., Boano et al., 2006) and lab-scale studies (Han & Endreny, 2013) identifying higher lateral exchange across meander necks. Changes in gradients along the longitudinal WSE profile have been shown to be well correlated with hyporheic exchange (Anderson et al., 2005). WSE also provides the boundary conditions for driving lateral exchange through the meander necks (Han & Endreny, 2013).

The key sUAS-derived products from this study are the WSE, NDVI maps, and vegetation- top elevation distributions along meanders. Although sUAS-based thermal infrared imagery is an emerging data type to indicate deeper GW discharge, preliminary handheld infrared data indicated discrete discharge was likely not an important process at this study site.

Data acquisition

Visible and near-infrared multispectral imagery were collected on 8-9 August 2016 to map high-resolution elevation, spatial distribution of vegetation and NDVI. The total flight area is represented by a rectangle of ~400 m along the river-corridor length and ~180 m wide. Details of the sUAS and cameras as well as additional flight details are highlighted in Supplemental Table S1. All cameras were mounted on a fixed bracket for near-nadir conditions. The multispectral camera flew at mid-afternoon with slightly cloudy conditions.

Photogrammetry from the visible camera (Sony A5100, Sony Industries) was used in a Structure-

from-Motion (SfM) mode to generate a digital surface map (which includes vegetation) using Agisoft Photoscan. The SfM workflow incorporated 11 surveyed ~1x1 m ground control points with a handheld Trimble Geo7x and Zephyr GNSS antenna (best manufacturer-reported accuracy of 1 cm) distributed along the edge of the anticipated capture area. The target size was sufficient for recognition at the anticipated pixel resolution (~1.5 cm). The imagery from the multispectral camera (MicaSense RedEdge, MicaSense Inc., Seattle, WA) was post-processed to create an orthomosaic of five spectral bands (center wavelengths and bandwidths of 475±10, 560±10, 668±5, 717±5, and 840±20 nm, respectively).

For the digital surface map created from photogrammetry, our focus was on WSEs to estimate the river gradient, the hydraulic gradient across the meander necks, river-reach topography, and vegetation-top elevations. To estimate WSEs, we visually identified the bank-water interface (denoted in orange in Supplemental Figure S1) and extracted the elevation from the digital surface map along each bank at ~1.5 cm intervals, as described in Woodget et al. (2015). Other simple threshold masks were attempted to delineate the water- land interface (i.e., normalized water difference index, NDVI, and near infrared), but did not generate better results. There was substantial noise in WSE estimates along particular reaches of individual banks, likely due to vegetation protruding over the water (see Supplemental Figure S2). When vegetation obscured the bank, the WSE of the opposite bank was substituted (see Supplemental Table S2). For remaining noise, we took the lower 25% quantile of all extracted WSE values (mean of 98 pts) along 1-m intervals, assuming that the noise was vegetation overhang and the WSE would be lower in elevation. This results in an upscaled but continuous longitudinal WSE profile. For sensitivity, maximum and minimum WSE values were also analyzed every meter. Changes in WSE along the reach were chosen by longitudinal river locations. If the river location exhibited noise in WSE, the closest WSE point along a reach without noise was chosen.

Our multispectral camera provides higher resolution than satellite-derived Landsat imagery (~0.06 m versus 30 m resolution, respectively; see Supplemental Figure S3). NDVI was extracted from the multispectral bands and basic spatial analysis was performed along the three upstream meanders, M1, M2, and M3 (labeled in Figure 1a). These three meanders

were highly sinuous (upper reach sinuosity of ~4.2). Farther downstream, meanders were less sinuous, making the meander necks less pronounced. For spatial analyses of each meander, we took the statistics (median and 25 and 75% quantiles) of the pixel values within 10-m diameter circles (~22,000 pixels/circle) located along ~5-m intervals along axes perpendicular to the meander necks (see Figure 2a). Similar analyses were performed on the digital surface map (~370,000 pixels/circle) to view surface elevation distributions along the same axes. The elevation changes correspond with changes in vegetation-top elevations.

Results and Discussion

Topography and Stream Profile Reconstruction

The high-resolution visible imagery and SfM-created digital surface maps at ~1.5 cm pixel resolution yielded elevation values at over 600 million points (Figure 1a). The comparison between the modeled surface and the 11 surveyed ground control points had a 3.8-cm mean absolute error, 4.4-cm root-mean-squared error, and 2.5-cm precision. The mean absolute error is less than aerial LiDAR (21 cm) (Legleiter, 2012) and approaches terrestrial laser scanners (2-6 cm) (Williams et al., 2014). Higher resolution imagery, dictated by flight altitude and camera sensor resolution, and/or higher-accuracy surveying could further improve the accuracy. The data show regions of changing WSE gradients along different lengths (Figure 1b). The longitudinal river distances are referenced to the farthest upstream point of the study area (downstream distance of 0 m in Figure 1b).

In the less sinuous portion along the study reach, (~550-860 m), the WSE gradient is steeper than other reaches and corresponds with the greater hillslope gradient in the NW-SE direction shown in Figure 1b. The WSE gradient flattens downstream of 860 m. In the sinuous regions (0-550 m and 880-1100 m), the WSE profile exhibits higher variability, due to the pool-riffle sequences seen in the thalweg elevation line (Supplemental Figures S2).

The changes in WSE gradients correspond with riffle sequences and are resolved every 1 m down the reach. The water-surface gradients for the individual meanders ranged from 0.0012- 0.0032 and whole reach slope was estimated as 0.0034, which was comparable with a surveyed slope of ~0.003 completed with a handheld Trimble Geo7x and Zephyr GNSS antenna. The agreement is remarkable, and the sUAS-derived river level provides a spatially continuous snapshot of WSE. To generate such a detailed GPS survey would take days, and would be confounded by daily changes in flow.

Vegetation Mapping and Analysis

Figure 2a shows the NDVI for the entire study area. The pixel size is ~6 cm given the flight elevation of ~90 m, and is smaller than the scale of individual riparian and upland shrubs at the site. The transition from riparian to upland vegetation was easily identified in the field and stands out in Figure 2a, and corresponds directly with less dense upland vegetation and the transition to the river corridor (> 1 m) seen in Figure 1a. Higher NDVI and denser vegetation also appear along the southwest region of the flight area (denoted by a plus sign in Figure 2a), corresponding to a high density of willows. Bright yellow patches along the river (NDVI ~0.5) coincide with gravel point bars in the orthomosaic seen in Figure 2b.

Overall, the sUAS-derived data had a mean NDVI value of 0.58, which is considerably larger than the mean of the satellite-derived NDVI of 0.27 (Supplemental Figure S3). The resulting satellite-derived NDVI may be biased downward due to how the satellite pixels (30-m resolution) incorporate open water, atmospheric corrections, and other factors currently under investigation.

Of interest is the appearance of greener vegetation in the meanders, particularly concentrated at the meander necks (Figures 2b). Figure 2b shows the visible orthomosaic of the upper three meanders, and Figure 2c-e shows the NDVI along the y-y' axis in Figure 2a. It has been shown that GW "shortcutting" can be enhanced through meander bends (Boano et al., 2006; Revelli et al., 2008) and, thus, we expected that most GW-SW exchange would occur through the narrowest part of each meander bend, where the subsurface hydraulic gradient would be at a maximum. This exchange then can support greater vegetation in the neck region, as root water uptake can more quickly be replenished than in the wider parts of the meander bend, assuming the hydraulic conductivity of the meander bend is not substantially different. Since this is an actively eroding and depositing river, sediment hydraulic conductivity will be heterogeneous, yet there is no reason to expect a systematic difference in meander neck/meander bend conductivities. Unlike the obvious vegetation differences near the point bars, the meander neck vegetation qualitatively did not appear different in species composition or shrub density to investigators in the field. However, it is clear in the visual image (Figure 2b) that there is more dense vegetation in each of the meander necks, which resulted in patches of higher NDVI values and vegetation-top elevations (Figures 2c-e).

To quantitatively investigate the anomalous areas near the meanders, where previous models show preferential GW-SW lateral exchange (Boano et al., 2006; Revelli et al., 2008), we plotted NDVI along the meander widths (Figure 2c-e). Meanders M1 and M2 show that the densest vegetation (e.g., NDVI peak) is located near the neck of the meander with gradual NDVI decreases farther from the neck. M2 shows a slight depression at the neck (y=0) which corresponds to a large percentage of pixels showing standing water (Supplemental Figure S4). All meanders exhibit noticeable NDVI decreases near the meander bends (positive along y-y' axis), likely driven by seasonal inundation and vegetation growth time (Perucca et al., 2006). The largest decline is in

meander M1, potentially because it is the farthest from the upland gradient seen in Figure 1b. In contrast, the NDVI distribution along the y-y' axis for meander M3 does not fit the patterns for M1 and M2, as it consistently decreased along the y- y' axis, with no noticeable concavity about the neck. M3 is closest to the valley wall, and therefore larger-scale topographically driven GW flow may also influence plant water availability in addition to meander bed hyporheic flowpaths.

Use of In-Stream Temperatures to Indicate GW-SW Exchange

It is expected that stream temperatures on the downstream side of the meander would display less daily variation in zones of substantial shortcutting through the meanders as the GW discharge would be more thermally buffered by its transition through the meander sediments. When the FO-DTS summary statistics (mean and daily standard deviation) are plotted on sUAS imagery (Figure 3), several areas stand out. A slightly colder mean temperature zone is mapped along the meander area in proximity to an abrupt break in slope along the northeast bank with exposed shale bedrock outcrop (Figure 3a). These thermal anomalies are small in magnitude—approximately 0.2 °C less than the warmest mean interface zones—but may be related to diffuse GW discharge to SW that is commonly found at slope breaks and geologic contacts (Winter et al., 1998). Relatively cold SW temperatures in the summer indicate GW discharge zones, while reduced streambed interface temperature variation can indicate either discharge or hyporheic return flows, the latter being expected to approximate current mean ambient bed interface temperature (Hare et al., 2015). Interface thermal anomalies driven by GW-SW exchange processes are typically small in larger rivers as the discharge signature is dominated by in-channel advective heat exchange, but differences of a similar magnitude to that found here have been used to successfully locate GW seepage in similarly sized stream systems (Briggs et al., 2012). Of interest is the appearance of discrete, more thermally buffered zones (Figure 3b) that appear to coincide with the meander-bend zone, most notably on the downgradient side of M2. The observance of thermal buffering on the downstream side of each meander, while small, further supports the conclusion that hyporheic meander bend "shortcutting" is occurring in these regions as evidenced by the apparent return flow influence on bed temperature variance.

Estimation of GW "Shortcutting"

Coinciding denser vegetation (as delineated by the NDVI) and thermal buffering suggest that GW shortcutting is occurring through the necks of the meander bends.

Furthermore, we know from the sUAS WSE that subsurface hydraulic gradients are largest near the necks due to short distances and the maximum head drop between upstream and downstream reaches of the stream. From Figure 1b, the estimated hydraulic gradients through the subsurface of the meander necks (i.e., perpendicular to y-y' lines) were 0.035, 0.016, and 0.025 m/m for M1, M2, and M3, respectively.

Measurements of hydraulic conductivity from piezometers in meander M3, which ranged from 0.1 to 30 m/d, combined with a geometric mean of 1.4 m/d and estimates of hydraulic gradients yield a GW flux through M3 of 0.04 m/d. Assuming similar hydraulic conductivities for meanders M1 and M2, the resulting fluxes were 0.049 and 0.022 m/d, respectively. For comparison, the flow through the East River at the time of the experiment was ~0.8 m^3/s, and assuming a representative stream width of 10 m and depth of ~0.5 m, the surface water flux was ~0.15 m/s, almost 5 orders of magnitude greater than the subsurface flux through the meander. This finding is consistent with laboratory studies (Han & Endreny, 2013) when scaled for hydraulic conductivity differences. While our estimates of GW flux are uncertain due to spatial variability in hydraulic conductivities, sUAS WSE provided robust estimates of hydraulic gradients, and NVDI and the vegetative-top elevations provide context to relate vegetation patterns and the magnitude of GW fluxes. Furthermore, the FO-DTS identification of potential "shortcutting" across the meander neck supports these sUAS- derived conclusions. It is also important to note that the marked differences in vegetation seen in the sUAS

images were undetected in the field, and could not be resolved from traditional remote sensing.

Limitations of the sUAS data

While sUAS imagery and derived products (the water surface profile and NDVI maps) provide high-resolution data, they are still subject to accuracy concerns. For reconstructed elevation maps from SfM, a common issue is surface doming caused by accumulated errors in camera radial distortion estimates (James & Robson, 2014). For our work, the fixed camera position, incurring variability in both pitch and roll, and the use of ground control points minimize such errors. Given the narrow lengths of the meander necks (~14-24m), we expect the vertical errors to be negligible from doming effects. Larger errors are likely generated from the methods of water surface selection and interface evaluation along the river-bank interface. Steep interfaces remains a challenge, often requiring manual editing (Javernick et al., 2014). Our WSE estimates generated by selecting the lower 25% quantile every meter attempt to address (1) incorrect estimates that may potentially misrepresent submerged river bed topography and (2) vegetation overhang biasing averages. For our site, the sediment and vegetation distributions allowed WSE estimates to be made along banks with less vegetation and gentle bank slopes. WSE selection along rivers with dense vegetation on both banks would require more careful selection process.

For NDVI, generating radiometrically corrected reflectance of each band across the orthomosaic is still an area of research in multispectral imagery (Laliberte et al., 2011). In our study, post-processing software incorporating a reflectance panel was utilized, but specific details of derived reflectance mosaics are proprietary. Generating datasets that can be compared between different sensors and potentially upscaled for satellite comparisons is a clear path for future research. The weakest corroboration of GW-SW exchange in this work is presented in the vegetative mapping of NDVI and potential relation to lateral GW-SW exchange. Studies have generated relationships at larger scales with satellite-derived products for NDVI with depth to GW (Zhou et al., 2013) and with vegetation biomass (Buchhorn et al., 2016). In our work, we analyzed the distribution of the meander NDVI and vegetation-top elevations that exhibits behavior similar to modeled biomass in meandering rivers (Perucca et al., 2006), but would require more detailed GW and geomorphologic data to adequately disentangle these drivers to better explain varying vegetation distributions. The potential for connecting vegetation with hydrologic states (e.g., soil moisture, depth to GW) and processes (e.g., lateral exchange, evapotranspiration) is promising, and we would suggest augmenting such multispectral maps with other traditional hydrologic (e.g., hydraulic conductivity) and biologic (e.g., biomass) measurement methods that can be spatially distributed for further scientific inquiry.

Conclusions

The application of sUAS for examining GW-SW exchange represents the next step in the application of remote sensing to environmental systems, bridging “on the ground” and satellite-based scales. In this work, sUAS were used to image surface topography, water levels, and vegetation at sub-decimeter scales rapidly and repeatedly. The development of continuous stream-elevation profiles from photogrammetry represents an important step forward in the identification of changes in the river hydraulic gradient. Stream topography derived from sUAS was used to estimate hydraulic gradients through meander bends, where the most exchange is likely to occur. Streambed interface FO-DTS data indicated areas of hyporheic return flow discharge in the meandering section, and when combined with hydraulic conductivity estimates from piezometers, hyporheic fluxes through the meander bends were shown to be present but orders of magnitude lower than the adjacent stream fluxes.

sUAS data were also used to explore the relationship between water meander shortcutting and

vegetation growth. NDVI resolution was better than 10 cm, capable of documenting individual plants. The coupling of topographic analysis with low-cost multispectral imaging delimited subtle differences in vegetation density that were not visible from the ground and further suggested potential for GW shortcutting driving vegetation density. Over the East River site, we collected ~25 million pixels of NDVI data; by comparison, a typical NDVI product from Landsat would yield at best ~130 pixels, smearing areas of dense riparian vegetation with low-density upland vegetation.

The development of sUAS for hydrologic investigations offers the potential to develop spatially distributed watershed data at low cost and at high spatial and temporal resolution. In this work, we focus on visible and multispectral imagery to improve our analysis of river gradient and hyporheic exchange.

Appendix

The AirCTEMPs team contributing members in alphabetical order: P. Adkins, J. Burnett, J. S. Selker, C. Sladek, C. Walter, S. Welsh, M. Wing.

Acknowledgments, Samples, and Data

We are thankful to the students and participants of the CUAHSI "Techniques for Stream-Groundwater Investigations" Workshop that took place 8-12 August 2016 at the Rocky Mountain Biological Laboratory (RMBL) facility in Crested Butte, Colorado for their field support and their keen interest in learning new techniques. Financial support for this collaborative effort and instrumentation was provided by the National Science Foundation through grants EAR-1440596, EAR-1440506, EAR-1338606, EAR-1446235 and Department of Energy grant DE-SC0016412. We thank Liz Tran (CUAHSI), Dr. Kenneth Williams (Lawrence Berkeley National Laboratory), Ian Billick and Jennie Reithel (RMBL) for important logistical support, and Jackie Randell (Colorado School of Mines) for field support. All flights were flown under the State of Nevada's Broad Area Certificate of Operations and approved by the Gunnison National Forest.

There are no real or perceived financial conflicts or other affiliations. Data supporting the conclusions can be found in the supplemental material. Fiber-optic distributed temperature sensing data for this manuscript are available from usgs.gov as specified in the reference list. Any use of trade, firm, or product names is for descriptive purposes only and does not imply endorsement by the U.S. Government.

DTS data (Briggs et al., 2017) are available online (https://doi.org/10.5066/F7J9658M). Any additional data may be obtained from HP (henryp@unr.edu).

References

Anderson, J. K., Wondzell, S. M., Gooseff, M. N., & Haggerty, R. (2005). Patterns in stream longitudinal profiles and implications for hyporheic exchange flow at the H.J. Andrews Experimental Forest, Oregon, USA. Hydrological Processes, 19(15), 2931– 2949. https://doi.org/10.1002/hyp.5791

Bingham, Q. G., Neilson, B. T., Neale, C. M. U., & Cardenas, M. B. (2012). Application of high-resolution, remotely sensed data for transient storage modeling parameter estimation. Water Resources Research, 48(8), W08520. https://doi.org/10.1029/2011WR011594

Boano, F., Camporeale, C., Revelli, R., & Ridolfi, L. (2006). Sinuosity-driven hyporheic exchange in meandering rivers. Geophysical Research Letters, 33(18), L18406. https://doi.org/10.1029/2006GL027630

Boano, F., Harvey, J. W., Marion, A., Packman, A. I., Revelli, R., Ridolfi, L., & Wörman, A. (2014). Hyporheic flow and transport processes: Mechanisms, models, and biogeochemical implications. Reviews of Geophysics, 52(4), 2012RG000417. https://doi.org/10.1002/2012RG000417

Briggs, M. A., Lautz, L. K., & Hare, D. K. (2014). Residence time control on hot moments of net nitrate production and uptake in the hyporheic zone. Hydrological Processes, 28(11), 3741–3751. https://doi.org/10.1002/hyp.9921

Briggs, M. A., Lautz, L. K., McKenzie, J. M., Gordon, R. P., & Hare, D. K. (2012). Using high-resolution distributed temperature sensing to quantify spatial and temporal variability in vertical hyporheic flux. Water Resources Research, 48(2), n/a–n/a. https://doi.org/10.1029/2011WR011227

Briggs, M. A., Lautz, L. K., & McKenzie, J. M. (2012). A comparison of fibre-optic distributed temperature sensing to traditional methods of evaluating groundwater inflow to streams. Hydrological Processes, 26(9), 1277–1290. https://doi.org/10.1002/hyp.8200

Briggs, M. A., Pai, H., Malenda, H., Randell, J., Singha, K., Tyler, S. W., & Williams, K. H. (2017). Fiber-optic distributed temperature data collected along the streambed of the East River, Crested Butte, CO, USA: U.S. Geological Survey Data Release. https://doi.org/10.5066/F7J9658M

Broshears, R. E., Runkel, R. L., Kimball, B. A., McKnight, D. M., & Bencala, K. E. (1996). Reactive Solute Transport in an Acidic Stream: Experimental pH Increase and Simulation of Controls on pH, Aluminum, and Iron. Environmental Science & Technology, 30(10), 3016–3024. https://doi.org/10.1021/es960055u

Buchhorn, M., Raynolds, M. K., & Walker, D. A. (2016). Influence of BRDF on NDVI and biomass estimations of Alaska Arctic tundra. Environmental Research Letters, 11(12), 125002. https://doi.org/10.1088/1748-9326/11/12/125002

Cardenas, M. B. (2015). Hyporheic zone hydrologic science: A historical account of its emergence and a prospectus. Water Resources Research, 51(5), 3601–3616. https://doi.org/10.1002/2015WR017028

Cardenas, M. B., Doering, M., Rivas, D. S., Galdeano, C., Neilson, B. T., & Robinson, C. T. (2014). Analysis of the temperature dynamics of a proglacial river using time-lapse thermal imaging and energy balance modeling. Journal of Hydrology, 519, 1963– 1973. https://doi.org/10.1016/j.jhydrol.2014.09.079

Dugdale, S. J., Bergeron, N. E., & St-Hilaire, A. (2015). Spatial distribution of thermal refuges analysed in relation to riverscape hydromorphology using airborne thermal infrared imagery. Remote Sensing of Environment, 160, 43–55. https://doi.org/10.1016/j.rse.2014.12.021

Eamus, D., Zolfaghar, S., Villalobos-Vega, R., Cleverly, J., & Huete, A. (2015). Groundwater-dependent ecosystems: recent insights from satellite and field-based studies. Hydrol. Earth Syst. Sci., 19(10), 4229–4256. https://doi.org/10.5194/hess-19- 4229-2015

Ebersole, J. L., Liss, W. J., & Frissell, C. A. (2003). Thermal heterogeneity, stream channel morphology, and salmonid abundance in northeastern Oregon streams. Canadian Journal of Fisheries and Aquatic Sciences, 60(10), 1266–1280. https://doi.org/10.1139/f03-107

Fuller, C. C., & Harvey, J. W. (2000). Reactive Uptake of Trace Metals in the Hyporheic Zone of a Mining-Contaminated Stream, Pinal Creek, Arizona. Environmental Science & Technology, 34(7), 1150–1155. https://doi.org/10.1021/es990714d

Gomez-Velez, J. D., Harvey, J. W., Cardenas, M. B., & Kiel, B. (2015). Denitrification in the Mississippi River network controlled by flow through river bedforms. Nature Geoscience, 8(12), 941–945. https://doi.org/10.1038/ngeo2567

González-Pinzón, R., Haggerty, R., & Argerich, A. (2014). Quantifying spatial differences in

metabolism in headwater streams. Freshwater Science, 33(3), 798–811. https://doi.org/10.1086/677555

González-Pinzón, R., Ward, A. S., Hatch, C. E., Wlostowski, A. N., Singha, K., Gooseff, M. N., … Brock, J. T. (2015). A field comparison of multiple techniques to quantify groundwater–surface-water interactions. Freshwater Science, 34(1), 139–160. https://doi.org/10.1086/679738

Han, B., & Endreny, T. A. (2013). Spatial and temporal intensification of lateral hyporheic flux in narrowing intra-meander zones. Hydrological Processes, 27(7), 989–994. https://doi.org/10.1002/hyp.9250

Hare, D. K., Briggs, M. A., Rosenberry, D. O., Boutt, D. F., & Lane, J. W. (2015). A comparison of thermal infrared to fiber-optic distributed temperature sensing for evaluation of groundwater discharge to surface water. Journal of Hydrology, 530, 153–166. https://doi.org/10.1016/j.jhydrol.2015.09.059

Harvey, J., & Fuller, C. C. (1998). Effect of enhanced manganese oxidation in the hyporheic zone on basin-scale geochemical mass balance. Water Resources Research, 34(4), 623–636. https://doi.org/10.1029/97WR03606

Harvey, J., & Gooseff, M. (2015). River corridor science: Hydrologic exchange and ecological consequences from bedforms to basins. Water Resources Research, 51(9), 6893–6922. https://doi.org/10.1002/2015WR017617

James, M. R., & Robson, S. (2014). Mitigating systematic error in topographic models derived from UAV and ground-based image networks. Earth Surface Processes and Landforms, 39(10), 1413–1420. https://doi.org/10.1002/esp.3609

Javernick, L., Brasington, J., & Caruso, B. (2014). Modeling the topography of shallow braided rivers using Structure-from-Motion photogrammetry. Geomorphology, 213, 166–182. https://doi.org/10.1016/j.geomorph.2014.01.006

Jin, X. M., Schaepman, M. E., Clevers, J. G. P. W., Su, Z. B., & Hu, G. C. (2011). Groundwater Depth and Vegetation in the Ejina Area, China. Arid Land Research and Management, 25(2), 194–199. https://doi.org/10.1080/15324982.2011.554953

Kalbus, E., Reinstorf, F., & Schirmer, M. (2006). Measuring methods for groundwater - surface water interactions: a review. Hydrology and Earth System Sciences, 10(6), 873–887. https://doi.org/10.5194/hess-10-873-2006

Kenwell, A., Navarre-Sitchler, A., Prugue, R., Spear, J. R., Hering, A. S., Maxwell, R. M., … Williams, K. H. (2016). Using geochemical indicators to distinguish high biogeochemical activity in floodplain soils and sediments. Science of The Total Environment, 563, 386–395. https://doi.org/10.1016/j.scitotenv.2016.04.014

Knapp, J. L. A., González-Pinzón, R., Drummond, J. D., Larsen, L. G., Cirpka, O. A., & Harvey, J. W. (2017). Tracer-based characterization of hyporheic exchange and benthic biolayers in streams. Water Resources Research, 53(2), 1575–1594. https://doi.org/10.1002/2016WR019393

Laliberte, A. S., Goforth, M. A., Steele, C. M., & Rango, A. (2011). Multispectral Remote Sensing from Unmanned Aircraft: Image Processing Workflows and Applications for Rangeland Environments. Remote Sensing, 3(11), 2529–2551. https://doi.org/10.3390/rs3112529

Legleiter, C. J. (2012). Remote measurement of river morphology via fusion of LiDAR topography and spectrally based bathymetry. Earth Surface Processes and Landforms, 37(5), 499–518. https://doi.org/10.1002/esp.2262

Loheide, S. P., & Gorelick, S. M. (2006). Quantifying Stream−Aquifer Interactions through the Analysis of Remotely Sensed Thermographic Profiles and In Situ Temperature Histories. Environmental Science & Technology, 40(10), 3336–3341. https://doi.org/10.1021/es0522074

Lucieer, A., Malenovský, Z., Veness, T., & Wallace, L. (2014). HyperUAS—Imaging Spectroscopy from a Multirotor Unmanned Aircraft System. Journal of Field Robotics, 31(4), 571–590. https://doi.org/10.1002/rob.21508

Lv, J., Wang, X.-S., Zhou, Y., Qian, K., Wan, L., Eamus, D., & Tao, Z. (2013). Groundwater-dependent distribution of vegetation in Hailiutu River catchment, a semi-arid region in China. Ecohydrology, 6(1), 142–149. https://doi.org/10.1002/eco.1254

Marzadri, A., Tonina, D., McKean, J. A., Tiedemann, M. G., & Benjankar, R. M. (2014). Multi-scale streambed topographic and discharge effects on hyporheic exchange at the stream network scale in confined streams. Journal of Hydrology, 519, 1997–2011. https://doi.org/10.1016/j.jhydrol.2014.09.076

Passalacqua, P., Belmont, P., Staley, D. M., Simley, J. D., Arrowsmith, J. R., Bode, C. A., … Wheaton, J. M. (2015). Analyzing high resolution topography for advancing the understanding of mass and energy transfer through landscapes: A review. Earth- Science Reviews, 148, 174–193. https://doi.org/10.1016/j.earscirev.2015.05.012

Perucca, E., Camporeale, C., & Ridolfi, L. (2006). Influence of river meandering dynamics on riparian vegetation pattern formation. Journal of Geophysical Research: Biogeosciences, 111(G1), G01001. https://doi.org/10.1029/2005JG000073

Revelli, R., Boano, F., Camporeale, C., & Ridolfi, L. (2008). Intra-meander hyporheic flow in alluvial rivers. Water Resources Research, 44(12), W12428. https://doi.org/10.1029/2008WR007081

Selker, J., van de Giesen, N., Westhoff, M., Luxemburg, W., & Parlange, M. B. (2006). Fiber optics opens window on stream dynamics. Geophysical Research Letters, 33(24), L24401. https://doi.org/10.1029/2006GL027979

Vander Jagt, B., Lucieer, A., Wallace, L., Turner, D., & Durand, M. (2015). Snow Depth Retrieval with UAS Using Photogrammetric Techniques. Geosciences, 5(3), 264–285. https://doi.org/10.3390/geosciences5030264

Wang, X., Xie, H., Guan, H., & Zhou, X. (2007). Different responses of MODIS-derived NDVI to root-zone soil moisture in semi-arid and humid regions. Journal of Hydrology, 340(1), 12–24. https://doi.org/10.1016/j.jhydrol.2007.03.022

Whitehead, K., & Hugenholtz, C. H. (2014). Remote sensing of the environment with small unmanned aircraft systems (UASs), part 1: a review of progress and challenges. Journal of Unmanned Vehicle Systems, 02(03), 69–85. https://doi.org/10.1139/juvs- 2014-0006

Williams, R. D., Brasington, J., Vericat, D., & Hicks, D. M. (2014). Hyperscale terrain modelling of braided rivers: fusing mobile terrestrial laser scanning and optical bathymetric mapping. Earth Surface Processes and Landforms, 39(2), 167–183. https://doi.org/10.1002/esp.3437

Winnick, M. J., Carroll, R. W. H., Williams, K. H., Maxwell, R. M., Dong, W., & Maher, K. (2017). Snowmelt controls on concentration-discharge relationships and the balance of oxidative and acid-base weathering fluxes in an alpine catchment, East River, Colorado. Water Resources Research, (53), n/a-n/a. https://doi.org/10.1002/2016WR019724

Winter, T. C., Harvey, J. W., Franke, O. L., & Alley, W. M. (1998). Ground water and surface water; a single resource (Circular 1139) (p. 79). US Geological Survey.

Woodget, A. S., Carbonneau, P. E., Visser, F., & Maddock, I. P. (2015). Quantifying submerged fluvial topography using hyperspatial resolution UAS imagery and structure from motion photogrammetry. Earth Surface Processes and Landforms, 40(1), 47–64. https://doi.org/10.1002/esp.3613

Zahawi, R. A., Dandois, J. P., Holl, K. D., Nadwodny, D., Reid, J. L., & Ellis, E. C. (2015). Using

lightweight unmanned aerial vehicles to monitor tropical forest recovery. Biological Conservation, 186, 287–295. https://doi.org/10.1016/j.biocon.2015.03.031

Zhou, Y., Wenninger, J., Yang, Z., Yin, L., Huang, J., Hou, L., … Uhlenbrook, S. (2013). Groundwater–surface water interactions, vegetation dependencies and implications for water resources management in the semi-arid Hailiutu River catchment, China – a synthesis. Hydrol. Earth Syst. Sci., 17(7), 2435–2447. https://doi.org/10.5194/hess-17- 2435-2013

Figures

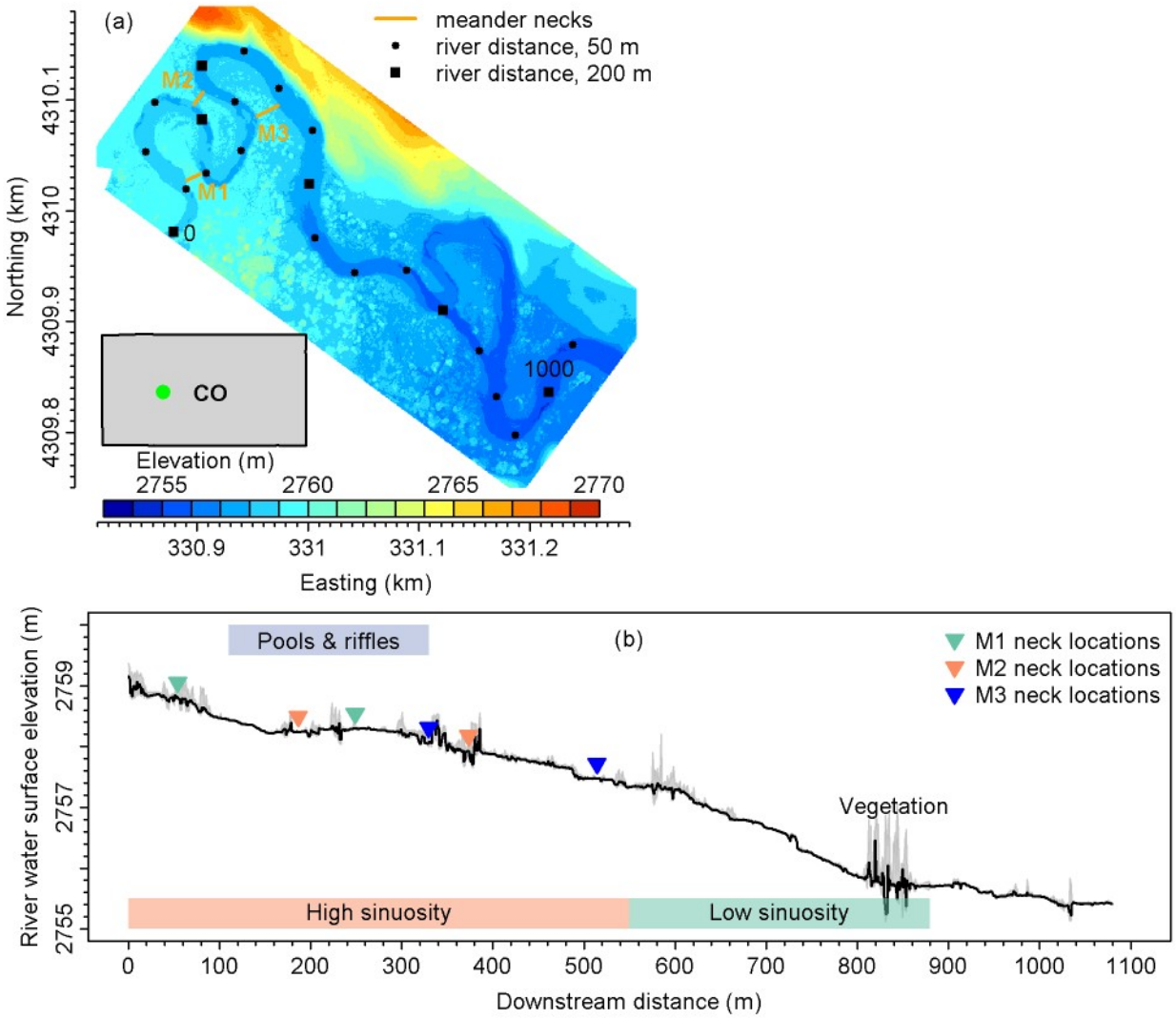

Figure 1. (a) The digital surface map with Colorado state inset in the bottom left and study location (green dot). (b) River WSE profile (black) extracted from the surface map (a) and treated for noise every meter (lower 25% quantile). Maximum and minimum WSE for every meter were included (grey shading in (b)) for sensitivity. The SfM estimations were made with Agisoft Photoscan v1.3.2.4205 using sUAS imagery captured at ~80-m elevation. Three river meanders (M1, M2, and M3) with easily identifiable river necks (orange lines) are discussed throughout this work and represent regions of likely GW-SW. Longitudinal river distances along the thalweg line are noted by points in (a). Squares correspond to major 200-m markers with the zero-point as an arbitrary upstream location. Circles in (a) represent 50-m increments. The distances in (a) correspond to the x-axis in (b). Longitudinal zones of high and low sinuosity, vegetation, and pool-riffle sequences (see Figure S2) are highlighted in (b). Triangles in (b) denote meander neck locations and are color-coded per meander (M2 downstream neck location was moved upstream by 6 m due to noise).

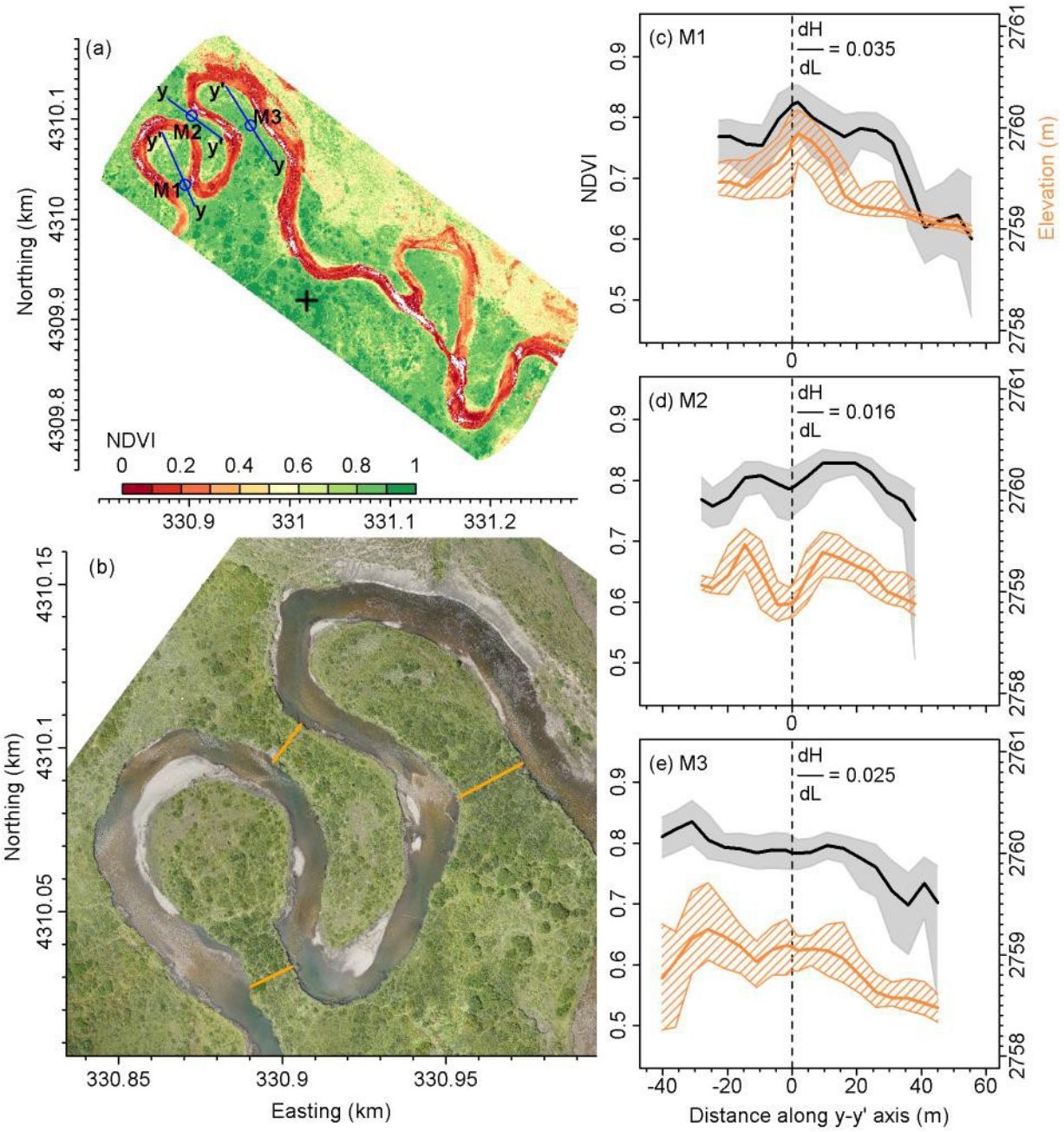

Figure 2. (a) NDVI estimates for the study reach. The locally elevated values of NDVI (greener) concentrated at the necks of the meanders. y-y' axes along meander widths with circles (zero-points) indicating the narrowest portion of the meander neck were used to generate the NDVI profiles shown in (c)-(e). White areas are where NDVI is less than 0. The large cross, "+", indicates the highest NDVI within our dataset. Note, the y-y' axes alternate orientation where y' represents the full bend and has positive values relative to the neck (0). (b) is the orthomosaic zoomed into the northwest with meander necks notated in orange. (c)-(e) show median NDVI (black) and elevation (orange) distributions along the y-y' axis with the 25% and 75% quantiles (grey and orange diagonals for NDVI and elevation, respectively), withthe hydraulic gradients (dH/dL) across the meander necks (dashed line) listed.

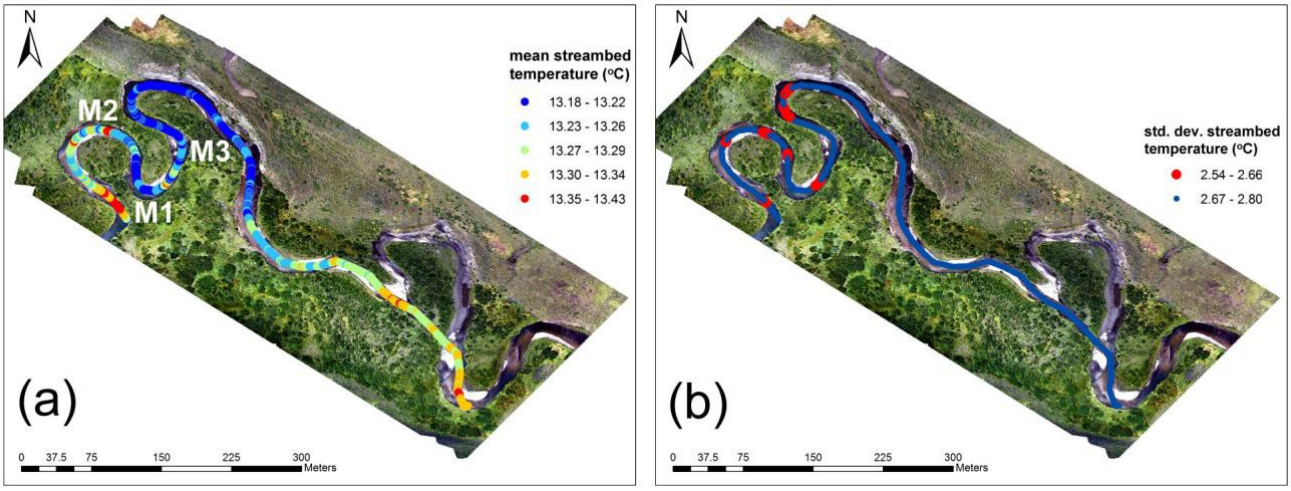

Figure 3. Fiber-optic distributed temperature sensing data are shown on georeferenced sUAS imagery with 21-day mean (a) and standard deviation (b) of streambed interface temperatures (°C). The larger red symbols in panel (b) indicate discrete thermally buffered zones that may indicate meander bend hyporheic return flows.